phys. stat. sol. (a) **202**, No. 15, 2858–2869 (2005) / **DOI** 10.1002/pssa.200521259

Deformation mechanisms of silicon during nanoscratching

R. Gassilloud[*, 1], **C. Ballif**[2], **P. Gasser**[1], **G. Buerki**[1], and **J. Michler**[1]

[1] EMPA, Materials Science and Technology, Feuerwerkerstrasse 39, 3602 Thun, Switzerland
[2] University of Neuchâtel, A.-L. Breguet 2, 2000 Neuchâtel, Switzerland

Received 23 August 2005, revised 26 September 2005, accepted 28 September 2005
Published online 22 November 2005

Dedicated to Professor Horst P. Strunk on the occasion of his 65th birthday

PACS 62.20Fe, 61.50Ks, 61.43Dq, 63.20Mt, 61.72Ff, 68.37Hk

The deformation mechanisms of silicon {001} surfaces during nanoscratching were found to depend strongly on the loading conditions. Nanoscratches with increasing load were performed at 2 μm/s (low velocity) and 100 μm/s (high velocity). The load-penetration-distance curves acquired during the scratching process at low velocity suggests that two deformation regimes can be defined, an elasto-plastic regime at low loads and a fully plastic regime at high loads. High resolution scanning electron microscopy of the damaged location shows that the residual scratch morphologies are strongly influenced by the scratch velocity and the applied load. Micro-Raman spectroscopy shows that after pressure release, the deformed volume inside the nanoscratch is mainly composed of amorphous silicon and Si-XII at low scratch speeds and of amorphous silicon at high speeds. Transmission electron microscopy shows that Si nanocrystals are embedded in an amorphous matrix at low speeds, whereas at high speeds the transformed zone is completely amorphous. Furthermore, the extend of the transformed zone is almost independent of the scratching speed and is delimited by a dislocation rich area that extends about as deep as the contact radius into the surface. To explain the observed phase and defect distribution a contact mechanics based decompression model that takes into account the load, the velocity, the materials properties and the contact radius in scratching is proposed. It shows that the decompression rate is higher at low penetration depth, which is consistent with the observation of amorphous silicon in this case. The stress field under the tip is computed using an elastic contact mechanics model based on Hertz's theory. The model explains the observed shape of the transformed zone and suggests that during load increase, phase transformation takes place prior to dislocation nucleation.

1 Introduction

Silicon (Si) is technologically the most important semiconductor material and therefore its electronic properties have been studied extensively in the past. The mechanical properties of silicon became a focus of research in the last ten years due to (a) the introduction of important mechanical semiconductor processing steps like thin wafer sawing for solar cells or separation of wafers bonding for silicon on insulator (SOI) technology and (b) the development of Micro Electro-Mechanical Systems (MEMS) based on silicon.

Indentation techniques, in particular nanoindentation, were widely used to study mechanical properties of silicon, mainly due to the capability to probe mechanical properties on a micro and nanoscale [1–6]. Silicon displays characteristic discontinuities upon loading ("pop-in") and unloading ("pop-out") in the load displacement curve [7, 8]. It is well accepted from high pressure cell studies that silicon transforms

* Corresponding author: e-mail: remy.gassilloud@empa.ch

from the cubic diamond phase (Si-I) to the metallic β-Sn phase (Si-II) at increased pressures [9, 10]. During pressure release, Si-II transforms to either an amorphous phase (a-Si) or to one of several high pressure polymorphs depending on experimental conditions. The pop-in, pop-out behaviour during indentation has been attributed to phase changes and associated density changes of the indented volume [11]. The understanding of the deformation mechanisms of silicon under nano- and micro-contact loading are a prerequisite to model and engineer abrasive processes like sawing or polishing as they govern the material removal mechanisms via local abrasive particle or asperity contacts. Nanoscratching would describe in many cases more accurately the local loading conditions in the abrasive process [2, 12]. The stress distribution below the scribing tip, however, differs significantly from nanoindentation experiments and the results from indentation cannot easily be transferred to nanoscratching. Furthermore, only few experimental work has been dedicated to crystalline structure analysis of silicon after nanoscratching [13, 14]. In this work, we investigated the formation of phases and defects during nanoscratching on silicon {001} surfaces depending on the applied load and the scratch speed. Raman spectroscopy and scanning and transmission electron microscopy were employed to characterise surface morphology as well as phases and dislocations distribution below the surface. Simple contact mechanics models are developed to explain the influence of scratch speed and the extend of phases and dislocations underneath the tip.

2 Experimental

For all nanoscratching experiments, double side polished Si(001) wafers were used. The wafers were first cleaved to samples of about 7 × 7 mm and the surfaces were scratched using a MTS Nano-Indenter XP equipped with a blunt diamond Berkovich tip (three sides with an apex angle of 65.3°). The diamond tip radius R was carefully characterized by atomic force microscopy (AFM). By extracting three profiles from a line lying along each edge of the blunt Berkovich tip and after averaging, the tip radius was evaluated to 2.4 to 3.7 μm, depending on the penetration of the tip during scratching. One edge of the Berkovich pyramid was facing the forward scratching direction. A linearly increasing load was applied from 0 to 50 mN along a total scratch length of 400 μm. The penetration depth varied correspondingly from 0 to about 350 nm, i.e. from nanoscratching to the micro-scratching conditions. For simplicity the term nanoscratching is employed in the following. Mainly two scratch velocities were investigated: 2 μm/s (low speed) and 100 μm/s (high speed). The initial grooves were obtained by scratching in the ⟨110⟩ crystalline direction. Nine samples were scratched, each composed of two nanoscratches performed at low and a high velocity.

High resolution scanning electron microscopy (SEM) micrographs were taken under a Hitachi 4800 operating at 5 kV. Cross-sectional transmission electron microscopy (TEM) lamellae were prepared using a focused ion beam (FIB) FEI Strata DB 235 installation. The cutting plane was a {110} plane perpendicular to the scratch direction. A Philips CM30 TEM operated at an acceleration voltage of 200 kV was used to study the microstructure of the TEM lamellae.

Micro-Raman spectroscopy was performed using a commercial Renishaw Ramascope 2000 spectrometer in the back-scattering configuration. The spectra were excited by the 632.8 nm line of Helium-Neon laser. The incoming light was focussed on the surface using a 100× microscope objective, and the scattered light was collected using the same objective. The spot size of the incident beam is estimated to be 1–2 μm, and the sampling depth is approximately 2.9 μm, based on the penetration distance of 632.8 nm (1.96 eV) light in silicon [15].

3 Results

Figure 1 shows the load-penetration-distance curves acquired in a scratching test at low velocity. Curve (a) and (b) represent the applied load and the penetration curve recorded during the scratching process, respectively. Curve (c) is the residual scratch profile after scratching. Inspection of the penetration curve recorded during loading (b) and the residual profile curve (c) after scratching indicates that the deforma-

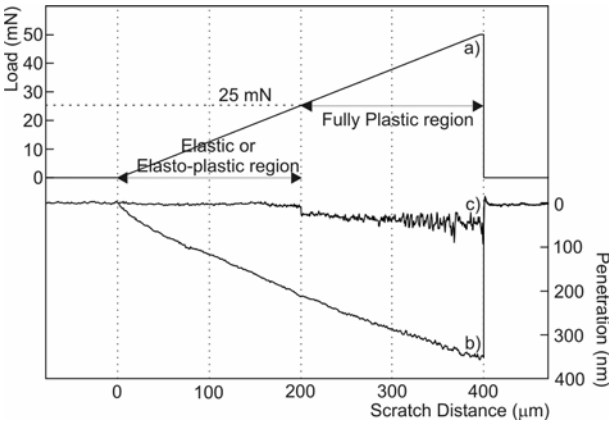

Fig. 1 Micro-scratching test performed at 2 μm/s velocity. (a) Load applied along a length of 400 μm, (b) the penetration curve recorded during the scratching process and (c) residual profile along the micro-scratch after the process.

tion can be separated into two regimes. Between 0 and 25 mN (i.e. 200 μm scratch distance), the deformation is elastic (eventually elasto-plastic). The penetration curve (b) follows approximately a square mathematical law as generally observable in a typical load-penetration curve of an indentation test. In this first region, the residual profile curve (c) is approximately constant, which signifies that during unloading the scratched surface returns to its original surface by elastic release. In contrast, between 25 and 50 mN (i.e. 200 μm to 400 μm), the penetration curve during loading (b) follows a linear law which indicates a transition from an elastic or elasto-plastic to a fully plastic regime. This transition is clearly visible in the residual profile curve and is characterized by a topographical step of ~20 nm at ~25 mN (i.e. 200 μm). From the measurement of the topographical step on nine identical load-penetration-displacement curves, an average value of 27 mN is obtained for this transition load. Beyond 25 mN (i.e. 200 μm), the depth and the roughness of the residual scratched surface increases with the applied load. To elucidate in more details the origin of the transition regime at 25 mN, the damaged locations were further studied via high resolution SEM.

Four samples were analyzed under high resolution SEM. The background image of Fig. 2 shows an overview SEM micrograph of the sample corresponding to curves of Fig. 1 at low velocity. The scratching direction is from the left to the right of the SEM image. The dark squares in the background picture are due to surface contamination. An omnipresent problem during SEM analysis of semiconductors is the rapid carbon contamination of the surface under the electrons beam. Conductive silver organic glue is

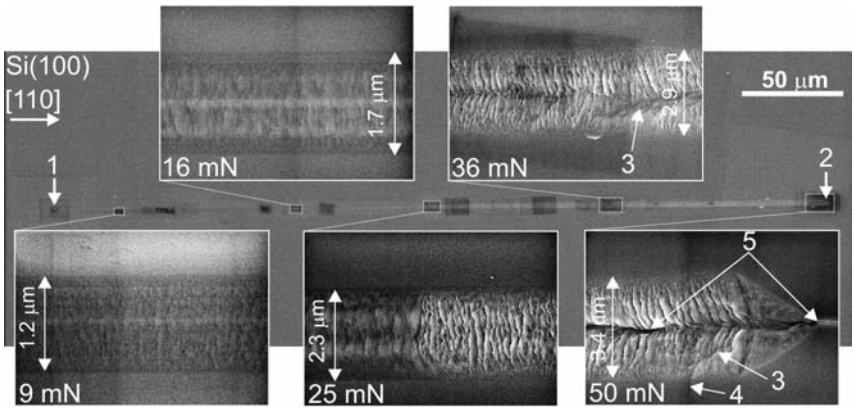

Fig. 2 General SEM micrograph of a 2 μm/s micro-scratch velocity (background picture). Arrow 1 indicates the beginning of the residual imprint, while arrow 2 the scratch end. Five magnified SEM micrograph insets are displayed at 9, 16, 25, 36, and 50 mN along the micro-scratch. Arrows 3, 4, and 5 shows micro-cracks in and outside the micro-scratch track.

required to hold the sample in the SEM microscope. We suspect that residues from this glue contaminate the surface during lift-off and are responsible for the carbon contamination. The contamination could be removed via plasma etching. However, an etching of the silicon surface could not be excluded. We found that the carbon contamination was useful to measure distances (and the subsequent applied load) along the scratch, by distance measurement from a contaminated area to the end of the scratch. Therefore, we decided to carry on the investigation with the contamination. Arrow 1 indicates the position of the scratch where the first residual imprint was visible under high resolution SEM imaging and arrow 2 point-outs its end. From the length measurement between arrow 1 and arrow 2, it is possible to evaluate the load required to create a first residual imprint at the surface. Based on an average of four scratches at low velocity, a mean value of 1.4 mN was found. Five magnified SEM micrograph insets at loads of 9, 16, 25, 36 and 50 mN are displayed along the nanoscratch of Fig. 2. These images show the influence of the load on the morphology of the residual nanoscratched surface. From 1.4 to 25 mN, the morphology consists of a rough surface with no defined structures. Neither cracks nor chips are generated during scratching in this region. Above 25 mN, a transition in the morphology is clearly visible, with the formation of "fish scale" micro-ridges. These micro-ridges denote material plastic flow following the tip during scratching as suggested at 50 mN. At this last load, the micro-ridges stop at the back side of the Berkovich residual imprint. The micro-ridges change in orientation along the nanoscratch. They start to be perpendicular to the scratch direction at 25 mN and finish to be more or less parallel to the scratching faces of the Berkovich tip. At 37 and 50 mN, micro-cracks are visible inside the nanoscratch (see arrow 3). At 50 mN, a perpendicular crack is visible outside the nanoscratch track (radial crack see arrow 4), and a crack at the edge of residual the Berkovich tip imprint is visible (see arrow 5) which indicates that a crack parallel to the scratching direction also called median crack may extend inside the bulk at the end of the nanoscratch.

Figure 3 shows the morphology of the high velocity nanoscratch. Here again, arrow 1 and 2 indicates the beginning and the end of the residual imprint of the nanoscratch, while the black squares are related to surface contamination. From the measurements of the distances between arrow 1 and arrow 2 on four scratches, the load, where the first residual imprint was observable under high resolution SEM, is evaluated to an average value of 2.7 mN. Four magnified micrographs of the nanoscratch at loads of 18, 25, 38, 50 mN are visible in Fig. 3. Direct morphology comparison at approximately the same loads can be performed with the low velocity experiment. It shows no noticeable difference in the morphology at 18 mN and 25 mN loads. It is even possible to say that the morphologies at these loads are almost the same. In addition, no sharp transition is observed at high velocity as visible at 25 mN in Fig. 2. At 38 and

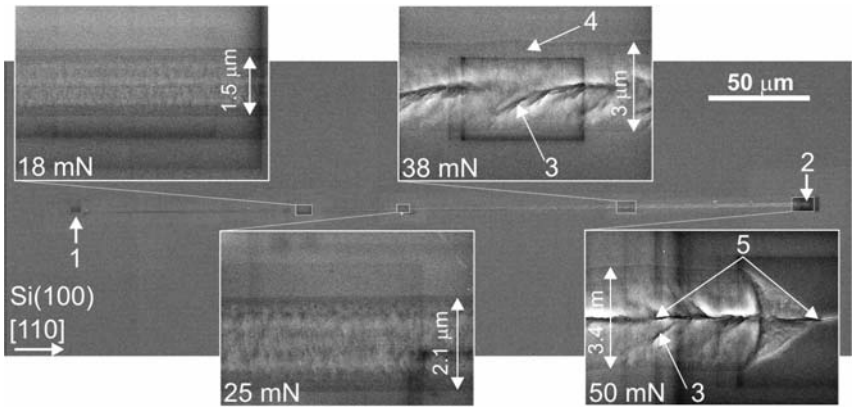

Fig. 3 General SEM micrograph of the 100 µm/s micro-scratch velocity (background image). Arrow 1 indicates the beginning of the residual imprint, while arrow 2 the scratch end. Five magnified SEM micrograph insets of the micro-scratch are displayed at 18, 25, 38, and 50 mN along the scratch. Arrow 4 shows plateaus where no deformed structures are visible. Arrows 3 and 5 point-out micro-cracks.

50 mN, the morphology of the residual imprint becomes very different from the low scratch velocity and is characterized by a smoothed surface in the middle of the nanoscratch surrounded by plateaus located at the borders with no deformed structures (see arrow 4). Finally, micro-cracks located in the flank of the residual scratch are visible (see arrow 3) as well as a parallel crack (median crack) at the end of the nanoscratch (see arrow 5).

From the SEM study, the following characteristics are reported: 1) at loads below 25 mN, the residual imprint morphologies for both velocities are almost identical, 2) no sharp transition at 25 mN is visible at high velocity, and 3) at loads above 25 mN, the residual morphologies of the nanoscratches are clearly different with micro-ridges formation at low velocity and smoothed features at high velocity. The loads required to let a first residual trace are approximately the same for both velocities and therefore it can be assumed to be independent on the scratch velocity.

To clarify the morphology differences observed between the two velocities, micro-Raman spectroscopy was used to characterize the crystalline structure of the surface inside the nanoscratch tracks. It is well known that during indentation, hydrostatic pressure (σ_{hydro}) can exceed the pressure limit to induce the phase transformation of silicon in the range of 8.8 to 16 GPa producing a new phase underneath the tip labeled Si-II (β-Sn structure), that is not stable at ambient pressure [9, 16–18]. This first transition is not reversible: Si-II transforms to different metastable phases depending on unloading conditions. In stepwise slow decompression, the first phase reported at $\sigma_{hydro} = 10-12$ GPa (~11.7 GPa) is Si-XII. On further release, Si-XII transforms to Si-III, producing a mixture of both phases, with Si-XII persisting at ambient pressure [2]. Si-III, and Si-XII have been reported to be stable after indentation tests in the residual imprints. Hence, these two metastables phase were intensively studied. To understand the Raman spectra of these phases, it is useful to recall the crystalline structure of these metastable phases. Si-III, also labeled as bc8, presents a body centered cubic structure with 8 atoms per primitive unit cell [19–21]. All atoms are tetrahedrally bonded with one short bond and three long bonds per atom (see crystallographic structure of Si-III in Fig. 8). At ambient pressure, the cubic cell dimension have been evaluated to $a_0 = 6.637$ Å [22]. Si-XII has been well investigated by Plitz et al. [23–25]. The phase has been denoted as r8, a rhombohedral structure with 8 atoms per primitive unit cell. The structures of r8 and bc8 are clearly related. Like bc8, it is characterized by distorted tetrahedral bonding with two distinct bond lengths (see crystallographic structure of Si-XII in Fig. 8). The cell dimension at ambient pressure has been evaluated to be $a_0 = 5.731$ Å. The ab initio calculation of Plitz et al. predicts five Raman-active modes for the bc8 structure, and height modes for the r8 structure [23]. As the r8 structure is considered to be a rhombohedral distortion of bc8, the two phases are expected to have similar Raman spectra. Indeed, the calculated phonon frequencies of r8 and bc8 differ by only ±10%, which makes difficult the separation of these phases based on the experimentally measured Raman spectra. Meanwhile, from experimental measurements, Ge et al. proposed that bands at 166, 184, 350, 375, 397, 435 and 485 cm^{-1} should be attributed to Si-XII, while the bands at 166, 384, 415, 433, 465 cm^{-1} to Si-III [26]. Finally, both Si-III and Si-XII are known to show semi-metallic electronic behaviors [27–29]. Other polymorph phases where reported from heat treatment of Si-III and in high pressure test experiments. They were labeled as Si-IV [13, 29] and Si-IX [30], and because they were not detected, they are not studied in the current work.

Figure 4 shows the micro-Raman spectra obtained from the 2 μm/s nanoscratch presented in Fig. 2. In background, an overview SEM micrograph is displayed and shows the location in the nanoscratch where Raman spectra were obtained. On all spectra, it is clearly seen that the single line at 521.7 cm^{-1} corresponding to the light scattered by a triply degenerated optical phonon in the centre of the Brillouin zone of the bulk Si-I. At loads below the morphological transition observed in Fig. 2 and Fig. 3 (i.e. 25 mN), the nanoscratch is composed of amorphous silicon (*a*-Si) as indicated by the broad band at approximately 465 cm^{-1}. The amount of *a*-Si is variable along the nanoscratch as indicated by the intensity ratio between the band at 465 cm^{-1} and 521.7 cm^{-1}, which increases with the load. Above the transition morphology at 25 mN, the nanoscratch is composed of the high pressure phase Si-XII, which is characterized by the bands at 354.1, 376.1, 399.2, 436.7, and 489.9 cm^{-1}. The band at 386.1 cm^{-1} predicted by Plitz et al. [23] for the bc8 structure, was attributed by Ge et al. [26] to Si-III together with other bands at 415

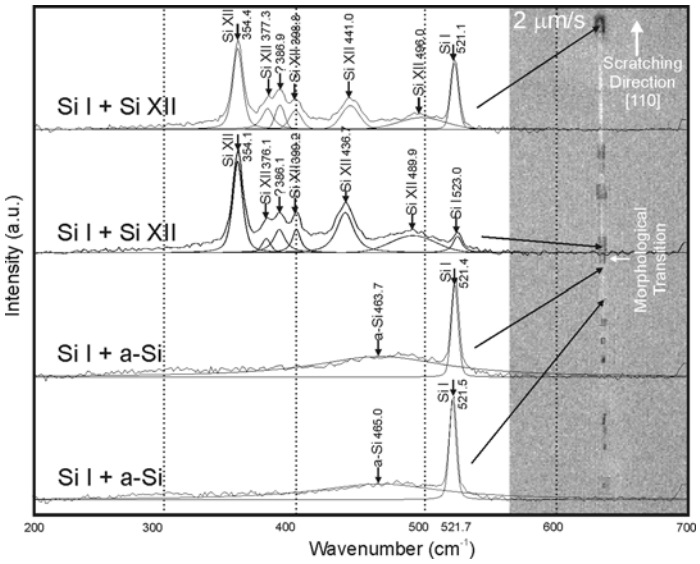

Fig. 4 Raman spectra acquired in the 2 μm/s micro-scratch. Before the morphological transition observed in Fig. 1 and Fig. 2, the micro-scratch is composed of *a*-Si, and after of Si-I and Si-XII. For illustration of the peak positions, we fitted the spectra with Gauss/Lorentz functions after a linear background correction.

and 465 cm^{-1}. However, the absence of these last bands would indicate that Si-III is in minor quantity in the nanoscratch track. Domnich et al. [2] proposed that in stepwise decompression, the first phase to form is Si-XII, with formation of Si-III under further pressure release producing a mixture of Si-III and a minor component of Si-XII at ambient pressure. The Raman spectra presented here, show that after pressure release, the nanoscratch is mainly composed of Si-XII, which does not follow the proposed decompression path by Domnich et al.

Figure 5 shows the Raman spectrum of the 100 μm/s scratch velocity visible in Fig. 3. The broad line at 465 cm^{-1} indicates that the full nanoscratch is composed of amorphous silicon. No polymorph phases were detected all along the nanoscratch residual track. Raman spectrum intensity ratio between the band at 465 and 521.7 cm^{-1} proposes that the amount of *a*-Si increases with the applied load. This can be easily explained, if one takes into account the presence of an amorphous layer at the nanoscratch surface. The Si-I band is arising from the crystalline silicon under the nanoscratch. As the load increases, the

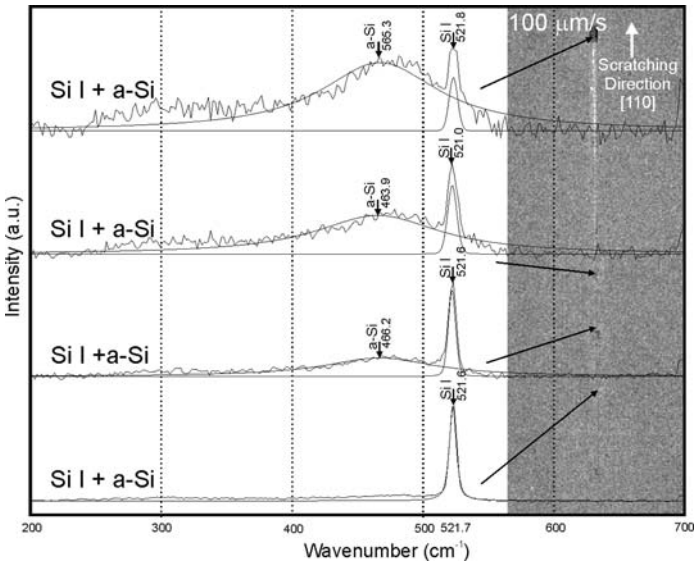

Fig. 5 Raman spectra acquired in the 100 μm/s micro-scratch of Fig. 5. All the micro-scratch is composed of *a*-Si as indicated by the broad band at 465 cm^{-1}. Si-I signal is from the bulk. For illustration of the peak positions, we fitted the spectra with Gauss/Lorentz functions after a linear background correction.

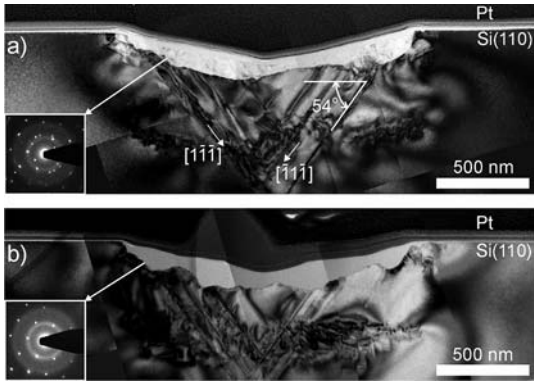

Fig. 6 a) and b) TEM bright field ([110] projection) cross-section perpendicular to the scratching direction of micro-scratches performed at 1 and 100 μm/s, respectively. Insets: Selected area diffraction (SAD) patterns of transformed layers at the micro-scratch surfaces.

thickness of the transformed layer increases and less signal is coming from the bulk silicon under the layer. To analyze the repartition and the amount of high pressure phases at the nanoscratch surfaces, the damaged locations were further investigated by cross sectional Transmission Electron Microscopy (TEM).

Figure 6(a) and (b) shows two cross sectional TEM bright field images perpendicular to the scratching direction with velocities of 1 and 100 μm/s, respectively. The scratches were performed at a constant load of 10 mN using a diamond Berkovich tip. As diamond tips wear generally rapidly during scribing of silicon and as the scribing experiments for TEM analysis in Fig. 6 were conducted prior to the experiments presented in Figs. 2 to 5, the tips radius was smaller. The tip was new, and the radius measured by AFM was approximately 200 nm. Consequently, at identical loads, the penetration of the tip is higher than the tip used in the SEM investigation. All other experimental conditions were identical to those presented in Figs. 2 to 5. From the evaluation of the nanoscratches width on the TEM micrographs (approximately 3 μm), it is assumed that the deformation regime corresponds to the loads above 25 mN in the SEM investigation. As will be shown below, the observed phases are coherent with this assumption. In both images, the platinum protective layer for FIB processing techniques can clearly be distinguished (denoted as Pt) as well as the V-Shape of the scratch corresponding to the ~120° open angle of the diamond Berkovich tip. The width and the depth of the residual imprints for both velocities are approximately identical, indicating that the residual sizes of the scratches are independent of the velocity, and most probably depend on the applied load. The striking difference between the two deformed microstructures presented, is the formation of a well defined region under the tip of a mixture of amorphous silicon and nanocrystallites of polymorph phases (see selected area diffraction pattern in Fig. 6(a) for the 1 μm/s velocity, whereas only amorphous silicon is seen at the same location (see diffraction pattern in Fig. 6(b)) for the 100 μm/s velocity. Such transformed material directly underneath the surface of the indenter was already reported in TEM investigation in indentation experiments [31–34]. It is generally assumed that the region of transformed silicon corresponds to the area of greatest hydrostatic pressure caused by the Berkovich tip [35–37]. The nanocrystalline material most likely contains a mixture of silicon phase Si-III and Si-XII as indicated by the Raman investigation. Due to the small size of transformed material under the tip, as well as the size of the nanocrystallites, identification of the phases through electron diffraction pattern indexing was not possible. Slip bands are clearly visible in both micrographs orientated at an angle of 54° to the {001} surface and therefore are aligned along the {111} equivalent planes. As the slip bands on the [1 $\bar{1}$ $\bar{1}$] and [$\bar{1}$1 $\bar{1}$] direction extend into the bulk, they intersect, which defines the characteristic V-shape of the dislocation distribution. It is interesting to note that similar to the width and to the depth of the residual imprint, the extension and density of dislocations seems to be independent from the scratch velocity and therefore most probably depends only on the applied load during scratching.

4 Discussion

Correlation of the load-penetration-distance curve at 2 μm/s (Fig. 1) with the high-resolution SEM investigation (Figs. 2 and 3) gives deeper insight into the sequence of phase transformations. In Fig. 2 and Fig. 3, at 9 and 16 mN, a clear trace of the nanoscratch is visible, but no residual impression is detected in the residual profile of the load-penetration-distance curve at the same loads. This suggests that in the load range between 1.4 and 25 mN, the deformation is either elasto-plastic with the formation of only a small plastic region surrounded by an elastically deformed volume or that an upward expansion due to a phase transformation would counterbalance the residual impression due to extensive plastic deformation.

The transition in morphology observed at 25 mN in Fig. 2, is also visible in the residual profile curve (Fig. 1(c)). This point-outs a noticeable change in the scratching regime. The micro-ridge structures observed beyond 25 mN were already reported in the works of Gogotsi et al., using a sharp pyramidal tip [13]. In the current case, in the inset at 25 mN in Fig. 2, the micro-ridges are clearly perpendicular to the micro-scratch direction, indicating that slightly above 25 mN, the contact is still spherical. In addition, careful inspection of the tip geometry measured by the AFM, confirmed that for the penetration slightly above 25 mN, the contact was still spherical. Our Raman investigation at low velocity shows that Si-XII is present when micro-ridges start to form, which indicates that the micro-ridge formation is linked to the kinetics of this phase transformation. Upon slow decompression, the Si-II $\rightarrow$ Si-XII transition leads to ~9% volume expansion [2] and therefore, expansion in volume of the deformed area during slow decompression may lead to the formation of the micro-ridges visible in Fig. 2. Therefore, micro-ridges are not due to a modification of the geometry of the contact, i.e. from spherical to a pyramidal contact, but by the formation of the Si-XII phase.

The equivalent morphological characteristics observed for both velocities at low loads (i.e. 18 mN and 25 mN) in the SEM investigation are due to amorphous silicon formation as suggested by the Raman spectra of Figs. 4 and 5. It is well admitted that polymorph phases are formed under slow decompression, whereas *a*-Si is formed under high decompression rate. Our Raman study shows, however, that for the low velocity, *a*-Si is formed prior to the polymorph phases. This behaviour was already reported in the work of Gogotsi et al. in the scratching of silicon, however not explained [13]. We may explain this behaviour with a simple contact mechanics model. Briscoe et al. proposed that the deformation velocity in scratching can be defined as the ratio of the scratching velocity to the scratching width [38, 39]:

$$\dot{\varepsilon}_s = \frac{v}{b}. \tag{1}$$

We extend the formula to take into consideration the mean contact pressure (P_m) under the tip to estimate the order of magnitude of the hydrostatic pressure below the tip, and therefore to estimate the decompression rate:

$$\dot{\sigma}_s \approx \frac{2vP_m}{b}, \tag{2}$$

where P_m is the mean contact pressure under the indenter defined as follows:

$$P_m = \frac{P}{A} = q\left(\frac{4P}{\pi b^2}\right), \qquad 1 \le q \le 2, \tag{3}$$

where P is the applied load, A the surface, R the tip radius, b the residual scratch width, and q a parameter which considers the material response in scratching. The coefficient "2" in Eq. (2), expresses the fact that the decompression takes place at the rear half of the contact circle. Briscoe et al. proposed that for rigid plastic material such as metals $q = 2$, and for materials such as polymers with high elastic release, $q = 1$ [38]. In this study, for loads below 25 mN, the elastic release is high and therefore it is assumed that $q = 1$. The scratch width b is directly measured from the SEM micrographs, and is used as basis for the estimation of the decompression rate. For $P = 25$ mN, $b = 2.34$ μm, and $v = 2$ μm/s, we compute

$\dot{\sigma}_s$ = 9.94 GPa/s. For a lower load, P = 9.4 mN, b = 1.19 μm, and the same velocity, we obtain $\dot{\sigma}_s$ = 28.6 GPa/s. This is consistent with the fact that amorphous silicon is formed at earlier load than high pressure phases because the decompression rate at load of 9.4 mN is approximately 3 times higher than at 25 mN. As a consequence, at low velocity and below 25 mN and at high velocity all along the nanoscratch, the residual morphology characterized by a smoothed surface is due to amorphisation of the crystalline silicon during scratching as confirmed by the Raman investigation. This explains why at low and high velocity below 25 mN, the morphologies of the nanoscratches are identical.

If this model gives an explanation for the appearance of the amorphous phase at low loads, it is difficult to understand the evolution of the hydrostatic pressure during scribing once the phase transformations (*a*-Si or *a*-Si + Si-XII) takes place as there is no analytical model that takes these effects into account. An analytical solution to the contact problem during scribing with spheres is, however, available for the purely elastic case. From the minimum load required to let a residual trace at the surface, it is possible for both velocities to evaluate the stress field under the tip using the equation set written by Hanson et al. [40, 41]. Hanson's model allows the calculation of the stress field of a static perfectly elastic spherical scratching on an isotropic half space. Actually, the equations model the static loading of a sphere obliquely to a plan. A friction coefficient was introduced by Hanson in his model and is used to calculate the transversal load from the applied normal load. Additionally, the indenter materials properties can be set up for higher accuracy in the results. We assume here that Hanson's model is valid until the limit between elasticity and elasto-plasticity. The deformation of silicon in indentation was extensively studied and showed that plastic deformation of silicon is due to indentation-induced phase transformation of the single crystal and dislocations-induced ductility due to the extremely high pressure achieved under the tip [1, 2, 32, 33]. On the one hand, under a high hydrostatic pressure, a first phase transformation takes place in monocrystalline silicon: semiconducting silicon (Si-I) transforms into the metallic state (Si-II). Transition occurs when the hydrostatic pressure ranges between 8.8 and 16 GPa [2]. This transition is a pre-requisite step to formed Si-XII depending on the pressure release conditions. The hydrostatic stress can be calculated under the tip using the equations of Hanson et al. and so the pressure required to induce first Si-I → Si-II transformation can be evaluated. On the other hand, the dislocations nucleation and propagation are known to be caused by the shearing stresses in single crystal semiconductors [42]. It is well known that in diamond structures dislocations glide on {111} equivalent planes [43–46]. Hence, the shear stress on the {111} planes, in the anisotropic case, would be the appropriate value to analyze the dislocations nucleation and propagation. Even if this case is covered by Hanson's equations, its implementation appeared difficult. Therefore, in this work, the maximum shearing stress has been chosen as the most suitable parameter to discuss the pressure required to nucleate the first dislocations in scratching. In addition, silicon is considered as an anisotropic semiconductor, although it has a reasonable low anisotropic factor, i.e. A = 1.55 [47]. In silicon, the theoretical critical shear stress required to nucleate first dislocations is between G/15.7 = 4.2 GPa and G/9.2 = 7.2 GPa, where G is the isotropic shear modulus [48].

Figure 7 shows the computed hydrostatic stress and the critical shear stress under the tip. For computation, the average transition load obtained on four scratching tests performed at 2 μm/s was employed i.e. the, 1.4 mN, together with 2.4 μm for tip radius and a friction coefficient of f = 0.1. Using E_{Diamond} = 1143 GPa [49], ν_{Diamond} = 0.07 [50], E_{Si} = 162 GPa [48], ν_{Si} = 0.22 [48], we calculate σ_{Hydro} = 8.3 GPa at the surface, τ_{crit} = 2.5 GPa at the surface, and τ_{crit} = 3.3 GPa in the bulk. As already reported, an analytical calculation of the stress fields shows the region of greatest hydrostatic pressure in Fig. 7(a) to be located in a shallow region directly beneath the indenter [32, 35]. The hydrostatic pressure calculated under the tip (i.e. 8.3 GPa) is roughly equal to the one reported in high pressure experiments (anvil cell) for the first Si-I → Si-II transition (i.e. 8.8 GPa). The shear stresses are at the maximum at a depth beneath the surface of approximately half of the contact radius of the indenter as in Fig. 7(b). The critical shear stresses calculated under the tip at the surface (i.e. 2.5 GPa) and in the bulk (i.e. 3.3 GPa) are both significantly lower than the smallest shear limit required to nucleate the first dislocations (i.e. 4.2 GPa). Hence, it is speculated that the first residual trace visible under high resolution SEM at 1.4 mN and 2 μm/s velocity is due to deformation induced by phases transformation and not by dislocations

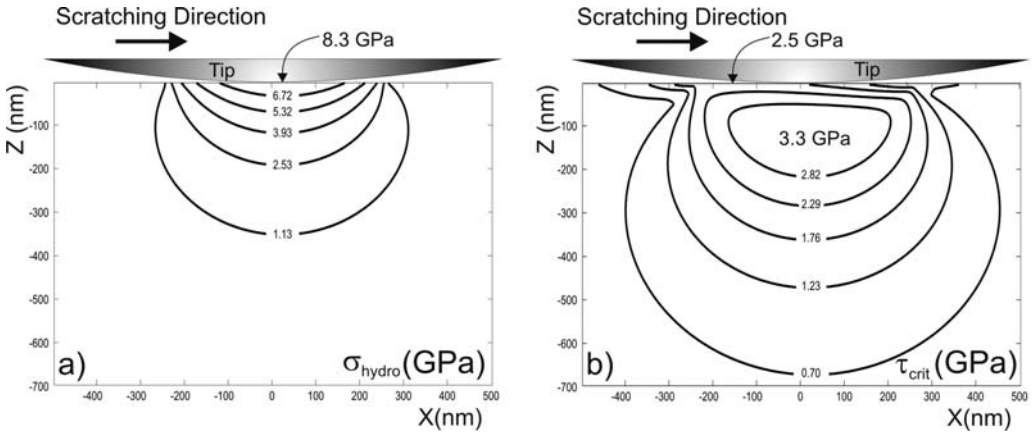

Fig. 7 Simulation of stress fields in the elastic regime under a spherical indenter of 2.4 μm radius loaded at 1.4 mN. (a) Hydrostatic pressure and (b) critical shear stress.

formation. For the high velocity, similar analysis has been performed and the results lead also to a lower value of the critical shear stress compared to the one requisite to initiate the first dislocations.

We suggest therefore a sequence for the deformation during scratching at low velocity which is easily extendable to high velocity where only amorphous silicon is formed. This is illustrated in Fig. 8. During the scratching process, firstly, the bulk silicon Si-I is loaded to approximately 1.4 mN. At this load a first transformation occurs, i.e. Si-II is formed since the hydrostatic pressure underneath the tip is more or less 8.8 GPa. Due to the high decompression rate (above 10 GPa/s) at low loads, amorphous silicon is firstly formed. Then, when the critical shear attains at least 4.2 GPa, first dislocations appear. Finally, the decompression rate decreases as the load increases until 10 GPa/s is reached. At this decompression rate, Si-II transforms to nanocrystallites of Si-XII (and maybe Si-III) embedded in an amorphous phase as visible from the TEM investigation.

5 Conclusion

Phase transformations and dislocations generation during the nanoscratching process on silicon {001} surfaces were studied. Two scratching parameters were analyzed: the applied load and the scratching velocity. It was shown that for a given tip radius, the applied load and the scratching velocity strongly influence the deformation mechanisms. The load-penetration-distance curves acquired during the scratching process at low velocity suggests that two deformation regimes can be defined, an elasto-

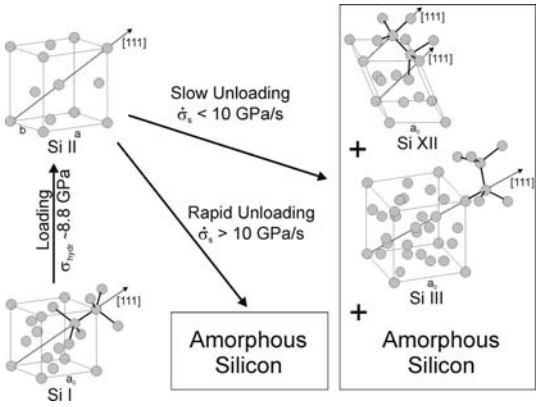

Fig. 8 Schematic of the phase transformation in silicon under dynamic loading.

plastic regime at low loads and a fully plastic regime at high loads. High resolution SEM of the damaged location shows that the residual scratch morphologies are strongly influenced by the scratching velocity and the applied load. Raman spectroscopy shows that after pressure release, the deformed volume inside the nanoscratch is mainly composed of *a*-Si and Si-XII at low scratch speeds and of *a*-Si at high speeds. Transmission electron microscopy revealed that the transformed zone is delimited by a dislocation rich area that extends about as deep as the contact radius into the surface. These observed mechanisms depend mainly on the decompression rate under the tip, which is calculated to be in the order of 10 GPa/s. At low load and constant velocity the decompression rate is estimated to be larger, leading to the formation of a layer of amorphous silicon. In contrast, at high load and constant velocity, the decompression rate decreases until it drops below a critical value. In such case, first polymorph phases are formed leading to a fully plastic deformation regime. It was found that the dislocations field extension and dislocation density is independent of the scratching velocity, which suggests that it is mainly related to the applied load for the studied indenter geometry. Finally, a calculation of the stress distribution in the elastic case of scratching suggests that amorphous silicon is formed prior to the initiation of the dislocations.

Acknowledgements The authors would like to thank Dr. K. Wasmer, and P. Pouvreau (EMPA Thun) for helpful discussions of the manuscript.

References

[1] N. V. Novikov, S. N. Dub, Y. V. Milman, I. V. Gridneva, and S. I. Chugunova, Sverkhtverd. Mater. **18**, 36 (1996).
[2] V. Domnich and Y. Gogotsi, Rev. Adv. Mater. Sci. **3**, 1 (2002).
[3] F. Demangeot, P. Puech, V. Domnich, Y. G. Gogtsi, S. Pinel, P. S. Pizani, and R. G. Jasinevicius, Adv. Eng. Mater. **4**, 543 (2002).
[4] A. Kailer, Y. G. Gogotsi, and K. G. Nickel, J. Appl. Phys. **81**, 3057 (1997).
[5] V. Domnich, Y. Gogotsi, and M. Trenary, Mater. Res. Soc. Symp. Proc. **649**, 8.9.1 (2001).
[6] V. Domnich, Y. Gogotsi, and S. Dub, Appl. Phys. Lett. **76**, 2214 (2000).
[7] J. E. Bradly, J. S. Williams, J. Wong-Leung, M. V. Swain, and P. Munroe, J. Mater. Res. **16**, 1500 (2001).
[8] E. R. Weppelmann, J. S. Field, and M. V. Swain, J. Mater. Res. **8**, 830 (1993).
[9] H. Olijnyk, S. K. Sikka, and W. B. Holzopfel, Phys. Lett. A **103**, 137 (1984).
[10] J. Z. Hu, L. D. Merkle, C. S. Menoni, and I. L. Spain, Phys. Rev. B **34**, 4679 (1986).
[11] Y. Gogotsi, V. Domnich, S. N. Dub, A. Kailer, and K. Nickel, J. Mater. Res. **15**, 871 (2000).
[12] Y. Gogotsi, C. Baek, and F. Kirscht, Semicond. Sci. Technol. **14**, 936 (1999).
[13] Y. Gogotsi, G. Zhou, S.-S. Ku, and S. Cetinkunt, Semicond. Sci. Technol. **16**, 345 (2001).
[14] A. Kovalchencko, Y. Gogotsi, V. Domnich, and A. Erdemir, Tribol. Trans. **45**, 372 (2002).
[15] I. de Wolf, Semicond. Sci. Technol. **11**, 139 (1996).
[16] G. J. Ackland, Rep. Prog. Phys. **64**, 483 (2001).
[17] H. Olijnyk, Phys. Rev. Lett. **68**, 2232 (1992).
[18] K. J. Chang and M. Cohen, Phys. Rev. B **48**, 7819 (1985).
[19] R. Biswas, R. M. Martin, R. J. Needs, and O. H. Nielsen, Phys. Rev. B **30**, 3210 (1984).
[20] M. T. Yin, Phys. Rev. B **30**, 1773 (1984).
[21] G. Weill, J. L. Mansot, G. Sagon, C. Carlone, and J. M. Besson, Semicond. Sci. Technol. **4**, 280 (1989).
[22] J. S. Kasper and S. M. Richards, Acta Cryst. **17**, 752 (1964).
[23] R. O. Plitz, J. R. Maclean, S. J. Clark, G. J. Ackland, P. D. Hatton, and J. Crain, Phys. Rev. B **52**, 4072 (1995).
[24] J. Crain, G. J. Ackland, J. R. Maclean, R. O. Plitz, P. D. Hatton, and G. S. Pawley, Phys. Rev. B **50**, 13043 (1994).
[25] J. Crain, G. J. Ackland, R. O. Plitz, P. D. Hatton, and S. J. Clark, J. Phys. Chem. Solids **56**, 495 (1995).
[26] D. Ge, V. Domnich, and Y. Gogotsi, J. Appl. Phys. **93**, 2418 (2003).
[27] J. M. Besson, E. H. Mokhtari, J. Gonzales, and G. Weill, Phys. Rev. Lett. **59**, 473 (1987).
[28] B. G. Pfrommer, M. Côté, St. G. Louie, and M. L. Cohen, Phys. Rev. B **56**, 6662 (1997).
[29] J. M. Besson, E. H. Mokhtari, J. Ganzales, and G. Weill, Phys. Rev. Lett. **59**, 473 (1987).
[30] Y.-X. Zhao, F. Buehler, J. R. Sites, and I. L. Spain, Solid State Commun. **59**, 679 (1986).
[31] D. L. Callahan and J. C. Morris, J. Mater. Res. **7**, 1614 (1992).

[32] J. E. Bradby, J. S. Williams, J. Wong-Leung, M. V. Swain, and P. Munroe, Appl. Phys. Lett. **77**, 3749 (2000).
[33] D. Ge, V. Domnich, and Y. Gogotsi, J. Appl. Phys. **93**, 2418 (2003).
[34] I. Zarudi and L. C. Zhang, Structure, Tribol. Int. **32**, 701 (1999).
[35] A. B. Mann, D. van Heerden, J. B. Pethica, and T. P. Weihs, J. Mater. Res. **15**, 1754 (2000).
[36] Y. Q. Wu, X. Y. Yang, and Y. B. Xu, Acta Mater. **47**, 2431 (1999).
[37] J. E. Bradby, J. S. Williams, J. Wong-Leung, M. V. Swain, and P. Munroe, J. Mater. Res. **16**, 1500 (2001).
[38] B. J. Briscoe, E. Pelillo, and S. K. Sinha, Polym. Eng. Sci. **36**, 2996 (1996).
[39] J. L. Bucaille, Simulation numerique de l'indentation et de la rayure des verres organiques, Thesis work (2001), presented at ENS Mines Paris France.
[40] M. T. Hanson, J. Tribol. **114**, 606 (1992).
[41] M. T. Hanson and T. Johnson, J. Tribol. **115**, 327 (1992).
[42] J. P. Hirth and J. Lothe, Theory of dislocations, 2nd ed. (John Wiley and Sons, New York, 1982).
[43] M. Azzaz, J.-P. Michel, and A. George, Philos. Mag. A **73**, 601 (1996).
[44] E. Le Bourhis, G. Patriarche, J. P. Riviere, and A. Zozime, phys. stat. sol. (a) **161**, 415 (1997).
[45] E. Le Bourhis and G. Patriarche, Eur. Phys. J. Appl. Phys. **12**, 31 (2000).
[46] G. Patriarche and E. Le Bourhis, Philos. Mag. A **82**, 1953 (2002).
[47] M. A. Meyers and K. K. Chawla: Mechanical behavior of materials (Prentice-Hall, Upper Saddle River, NJ, 1999).
[48] D. Lorenz, A. Zeckzer, U. Hilpert, P. Grau, H. Johansen, and H. S. Leipner, Phys. Rev. B **67**, 172101 (2003).
[49] P. Hess, Appl. Surf. Sci. **106**, 434 (1996).
[50] G. Simmons, and H. Wang, Single Crystal Elastic Constants and Calculated Aggregate Properties: A Handbook (MIT Press, Cambridge, Mass., 1971).

